

## Article

# Bacteria-Driven Fossil Ecosystems as Paleoindicators of Active Continental Margins and the Role of Carbonate Sediment-Hosted Vents in Geodynamic Reconstructions

László Bujtor <sup>1</sup>, Ildikó Gyollai <sup>2,3</sup>, Máté Szabó <sup>2,3</sup>, Ivett Kovács <sup>2,3</sup> and Márta Polgári <sup>1,2,3,\*</sup>

<sup>1</sup> Institute of Geography and Environmental Sciences, Eszterházy Károly Catholic University, 6-8 Leányka Street, H-3300 Eger, Hungary; bujtor.laszlo@uni-eszterhazy.hu

<sup>2</sup> HUN-REN Research Centre for Astronomy and Earth Sciences, Institute for Geological and Geochemical Research, Budaörsi út 45, H-1112 Budapest, Hungary; gyollai.ildiko@csfk.org (I.G.); szabo.mate@csfk.org (M.S.); kovacs.ivett@csfk.org (I.K.)

<sup>3</sup> HUN-REN Research Centre for Astronomy and Earth Sciences, MTA Centre of Excellence, Konkoly Thege Miklós út 15-17, H-1121 Budapest, Hungary

\* Correspondence: rodokrozit@gmail.com

**Abstract:** Continental rifting of the Tisza microplate started during the Late Jurassic and resulted in phreatic eruptions, peperite, and the construction of a volcanic edifice in the Early Cretaceous in the Mecsek Mountains (South Hungary). In the SE direction from the volcanic edifice at Zengővárkony, a shallow marine (depth 100–200 m) carbonate sediment hosted a vent environment, and iron ore deposition occurred at the end of the Valanginian to early Hauterivian, hosting a diverse, endemic fauna of approximately 60 species. The detailed mineralogical analysis of the transport conduits included Fe oxides (ferrihydrite, goethite, hematite, and magnetite), quartz, mixed carbonate, pyrite, feldspar, Fe-bearing clay minerals, apatite, sulfates (barite, gypsum, and jarosite), and native sulfur. Filamentous, microbially mediated microtextures with inner sequented, necklace-like spheric forms (diameter of 1  $\mu\text{m}$ ) and bacterial laminae are also observed inside decapod crustacean coprolites (*Palaxius tetraochearius*) and in the rock matrix. This complex ecological and mineralogical analysis provided direct evidence for the presence of bacteria in fossil sediment-hosted vent (SHV) environments on the one hand and for the intimate connection between bacteria and decapod crustaceans in hydrothermal environments 135 Ma before. This observation completes the fossil food chain of chemosynthesis-based ecosystems, from primary producers to the top carnivores reported for the first time from this locality.

**Keywords:** chemosymbiotic fossil ecosystem; food chain; low-temperature venting; Valanginian–Hauterivian; Tisza microplate; bacteria–decapod dependence; mineralogy



**Citation:** Bujtor, L.; Gyollai, I.; Szabó, M.; Kovács, I.; Polgári, M. Bacteria-Driven Fossil Ecosystems as Paleoindicators of Active Continental Margins and the Role of Carbonate Sediment-Hosted Vents in Geodynamic Reconstructions. *Minerals* **2024**, *14*, 125. <https://doi.org/10.3390/min14020125>

Academic Editor: Hiromi Konishi

Received: 30 November 2023

Revised: 17 January 2024

Accepted: 22 January 2024

Published: 24 January 2024



**Copyright:** © 2024 by the authors. Licensee MDPI, Basel, Switzerland. This article is an open access article distributed under the terms and conditions of the Creative Commons Attribution (CC BY) license (<https://creativecommons.org/licenses/by/4.0/>).

## 1. Introduction

The ecology, fauna, and geology of hydrothermal vents were immediately considered in the field of geoscience after the discoveries of recent [1] and fossil [2] representatives. These “classic” hydrothermal vent ecosystems have substrates of exposed rocks with limited or no sediment cover and are located at water depths less than 2000 m with fluid flow rates ranging from 0.1–6.2 m/s [3]. However, shallow marine (<200 m) counterparts are rare. Beaulieu and Szafranski [4] reported only 55 hydrothermal vents with water depths less than 150 m from 722 recent localities (7.6%), indicating limited occurrence of shallow marine venting; this conclusion was supported recently by [5], who reported forty-nine sites, of which only three were considered shallow marine. These types are characterized by very low flow rates ranging from 0.0001 m/s to 0.15 m/s [6] and are usually associated with sediment cover. Approximately 20 vent sites are known to exist within the water depth range of 100 to 200 m [7]. In many cases, geothermal and sedimentary domains can overlap,

leading to hybrid geological systems. These hybrid systems are known as sediment-hosted geothermal systems or sediment-hosted hydrothermal systems [8]. This terminology refers to sedimentary basins perturbed by magmatic intrusions or involved in volcanic plumbing systems. Experts dealing with venting are born on plate margins and use other terminology, e.g., sediment-hosted vents (SHV) [9]. We use the latter term because this term exclusively represents hydrothermal vents that are related to sediment cover and are directly related to rifting and volcanic processes, either at plate margins or within plate positions. Sediment-hosted shallow marine vents are rare but likely to promote chemosynthetic microbial activity and generate an enhanced food supply for infauna compared with background environments, as [10] presented and later confirmed [11]. The majority of known recent SHV environments are reported at water depths greater than 500 m [12].

The recent SHV communities are rare, as are their fossil counterparts. The first census on chemosymbiotic fossil ecosystems [13] reported 59 occurrences, of which only 13 ancient hydrothermal localities are known. Even a recent census [5] did not refer to significantly more recent SHV occurrences.

Proteobacteria play a major role in recent deep-sea hydrothermal vent ecosystems [14] and play an important role in SHV biota, irrespective of whether they oxidize or reduce sulfur. Sulfur-oxidizing chemolithotroph bacteria in hydrothermal environments are considered cosmopolitan in recent deep-sea vents [15] because of the wide range of electron donors and/or acceptors available for their biological activities, as (Table 2 in [7]) demonstrated.

Prokaryotes can produce widely different sulfur isotope fractionations during sulfate reduction [16]. Bacterial sulfide oxidation was long considered impossible; however, based on recent research [17] reporting that *Desulfurivibrio alkaliphilus* generates a consistent enrichment of sulfur  $-32$  as low as  $-34\text{‰}$   $\delta^{34}\text{S}$  seems to be feasible. This observation challenges the consensus that the microbial oxidation of sulfide does not result in large  $^{34}\text{S}$  enrichments and may provide a plausible explanation for the presence of highly negative  $\delta^{34}\text{S}$  measurements in fossil SHVs. In the following, we summarize the recent knowledge on the fossil SHV environment, highlighting the scope and background of our research.

The tiny depositional iron ore body at Zengővárkony (Mecsek Mountains, South Hungary) was discovered by Mr. Rezső Dezső, a private entrepreneur who made magnetic inclination measures in the 1930s. After World War II, the Hungarian State opened an ore mine that produced approximately 24,850 tons of iron ore between 1954 and 1956 [18]. Scientific research has also started [19], and a rich microfossil content was reported by [20]. This material was analyzed by [21], who reported six new crustacean microcoprolite ichnospecies. Iron ore generation was linked to early volcanic activity in the region [22]. Fülöp in [23] reported macrofossils from the dumps of the ore mine (ammonites, belemnites, brachiopods, echinoids, crinoids, and gastropods) and considered their age late Valanginian. A synthesis of the geological evolution of the region was provided by [24,25]. Bércziné et al. [26] included the Zengővárkony area in a paleogeographic reconstruction and located it in a shallower environment; however, they did not discuss the ore body and neglected to include it in a broader geological context.

Regarding the age of the succession, [27] used belemnites and dinoflagellate cysts to determine the age of the succession and concluded a late Valanginian to earliest Hauterivian age, confirming Fülöp in [23].

Bujtor [28] reported a rich brachiopod fauna from the locality that revealed a striking increase in size. Bujtor [29] proposed a venting or seeping origin, while [30] proposed a hot/warm hydrothermal origin; however, later, they proposed the idea of venting or seeping [31] and considered the succession of hydrothermal sediments, and [31] made sulfur stable isotopes from the Zengővárkony SHV (Figure 1). The authors obtained  $\delta^{34}\text{S}$  isotopic values of  $-35.9\text{‰}$  and  $-28.0\text{‰}$ . Bujtor and Nagy [32] also made sulfur isotope measurements that were in line with [31], and all the samples provided data from  $-40.4\text{‰}$  to  $-19.3\text{‰}$   $\delta^{34}\text{S}$ .

Rhombohedral calcite is present together with quartz-amethyst as holohedral crystal nests alongside the sulfide channels (Figure 2). Jáger et al. [31] reported that the mean temperature of primary fluid inclusions was 129 °C (range 98–145 °C), which does not contradict the observed temperature range of recent vent localities from that water depth [33].

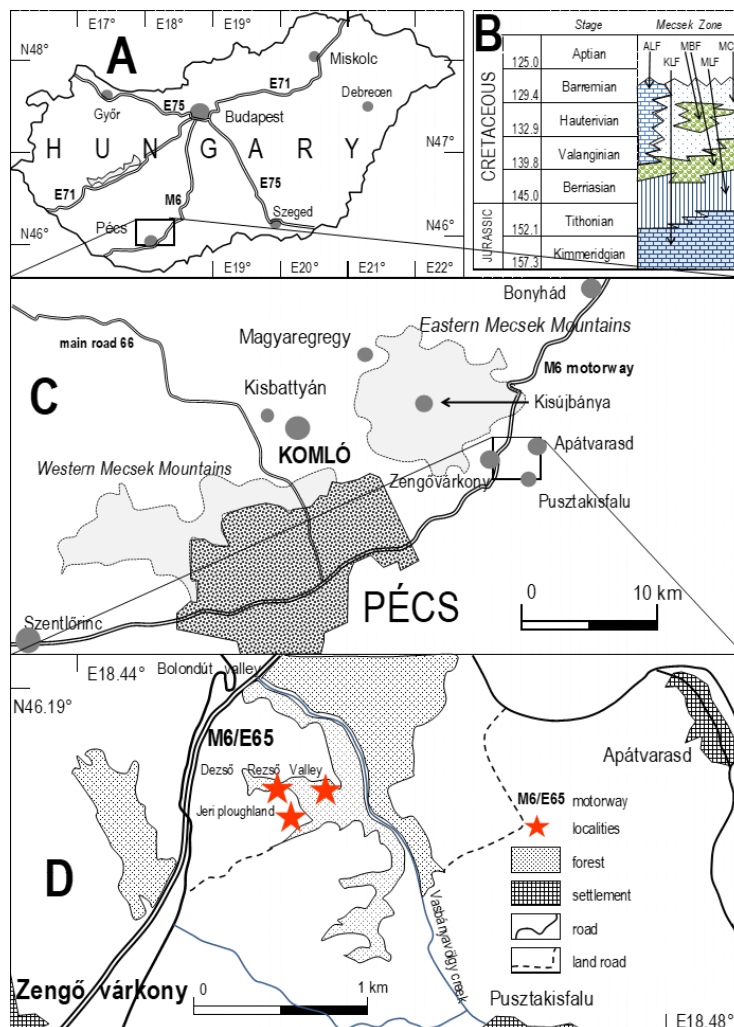


**Figure 1.** Map of the study area with a stratigraphic outline. (A) Simplified map of Hungary. The black border rectangle indicates the study area. (B) Lithostratigraphy of the Mecsek Zone for the study period. Numerical ages after [34]. Legend: ALF: Apátvarasd Limestone Fm; KLF: Kisújbánya Limestone Fm; MBF: Mecsekjánosi Basalt Fm; MCF: Magyaregregy Conglomerate Fm; MLF: Márévár Limestone Fm. (C) The study area relative to the Mecsek Mountains. The black border rectangle indicates the study area. (D) Zengővárkony area. Asterisks indicate the localities in the Dezső Rezső Valley and the Jeri ploughland.

Bujtor and Nagy [32] concluded that the most plausible water depth for the Zengővárkony environment could have been between 100 and 200 m (Figure 13 in [32]). From a water depth range between 200 and 400 m, only 16 active hydrothermal vent localities have been reported (Figure 4 in [33]) out of 521 localities (=3%), indicating a rare position for the Zengővárkony SHV.



**Figure 2.** Rhombohedral calcite crystals and holohedral quartz-amethyst crystals grew on the pillow lava surface alongside the fluid transport conduits. The sampling point coordinates are  $46.1851^{\circ}$  N,  $18.4553^{\circ}$  E. Scale bars indicate 1 cm.

Understanding the genesis of the Early Cretaceous iron ore was ambiguous for several decades. The first evidence of iron ore formation at this water depth in similar marine environments was obtained by [35]. This iron ore formation in SHV environments is from a similar geodynamic system in the Aeolian Islands, Tyrrhenian Sea, Italy, where at water depths between 80 and 400 m, there is an active fault system through which hydrothermal fluids enter the sea floor at temperatures ranging from 40 to 140 °C [36]. This thermal environment is strongly correlated with the Zengővárkony SHV. However, the faunal compositions of Zengővárkony and its counterpart at Panarea Island are generally similar, but the lack of decapod crustaceans at Panarea and the diverse decapod crustacean microcoprolites at Zengővárkony must be explained. Decapod crustaceans are the most important constituents of recent deep-sea hydrothermal vents [37] and are the primary consumers in the food chain. At Zengővárkony, the decapod crustacean microcoprolite ichnofauna is the most diverse species of the Mesozoic [32].

Although rich and diverse decapod crustaceans live on deep-sea hydrothermal vents, they are not the same on shallow marine soft substrates where burrowing decapods are frequent around the venting area [38] and are ghost shrimp (Callianassidae) that produce 10-channelled microcoprolites [39]; however, matching them with their host species is ambiguous, as [40,41] noted. The Zengővárkony locality indicates a fossil environment similar to that of the recent one at Milos Island, Greece [38,42]: at the center of the SHV, primary mineral formation occurred, and transport conduit packets developed through the unconsolidated carbonate sediments; at the soft lime ooze, apron decapod crustaceans lived, and they are considered neighboring heteropic biofacies. Two questions remain to be answered. First, where are the bacteria that are the primary producers of this fossil ecosystem? Second, how was the Fe enrichment (iron ore, indication) formed?

The aim of this paper is to present a novel mineralogical and detailed elemental analysis of this environment, including elemental maps and a proven connection between primary producers (bacteria) and primary consumers (decapod crustaceans). We propose that carbonate sediment-hosted vent environments are useful indicators for identifying fossil active plate margin areas in geological records.

## 2. Materials and Methods

### 2.1. Materials

Materials were collected chiefly during the field campaigns between 2010 and 2013, with occasional later recollections in 2016, out of which 5 samples were selected for the results described in Table 1.

**Table 1.** Lithological descriptions of the selected samples and the applied methods. Abbreviations: OM: optical rock microscopy; XRD: X-ray powder diffraction; FTIR: infrared spectroscopy; SEM–EDS: electron probe microanalysis. The number in brackets shows the number of spectra acquired by SEM–EDS; map: elemental map. The samples and thin sections are shown in Figure S1.

Sample No.	ID Number	Sampling Site	Description	Used Methods			
				XRD	OM	FTIR	SEM (EDS)
1	1	SE, Dezső Rezső Valley, Zengővárkony, Mecsek Mountains	Weathered sample fragments from hydrothermal channels through the nonconsolidated lime mud during venting.	1	44	64	26 (107) 4 maps
2	4	SE, Dezső Rezső Valley, Zengővárkony, Mecsek Mountains	Packet of hydrothermal channels nested in and among calcite-quartz mineral nests developed on the volcanite surface.	1	25	34	6 (40)
3	9	Jeri plowland S of Dezső Rezső Valley, Zengővárkony, Mecsek	Peperite sample block from the plowland revealing purple-colored micrite, biogenic fragments (mainly echinoderms) and altered volcanite grains with a greater fragment of a bivalve shell.	1	20	25	5 (28)
4	12	NW Dezső Rezső Valley, Zengővárkony, Mecsek Mountains	Metasomatized limestone block.	1	21	26	6 (28)
5	13	NW Dezső Rezső Valley, Zengővárkony, Mecsek Mountains	Sample of a partly metasomatized limestone block revealed purple-colored micrite with mudstone texture.	1	37	23	10 (28) 4 maps
Total	5			5	147	172	53 (231) 8 maps

Repositories. The analyzed samples and thin sections with their accompanying host rocks were deposited at the Rock Archive of EKKE (6 Leányka Street, H-3300 Eger, Hungary), Building D, Room 115, and Box D103; ID numbers: 2662 (sample 1), 2665 (sample 2), 2670 (sample 3), 2673 (sample 4), and 2674 (sample 5).

## 2.2. Applied Methods

### 2.2.1. Optical Rock Microscopy (OM)

Petrographic structural-textural studies were performed on 5 thin sections in transmitted and reflected light (NIKON ECLIPSE 600 rock microscope, IGGR RCAES HUN-REN, Budapest, Hungary). A total of 147 photos were taken.

### 2.2.2. X-ray Powder Diffraction (XRD)

The bulk mineralogical compositions of the 5 samples were analyzed by a Rigaku Miniflex-600 X-ray diffractometer with CuK $\alpha$  radiation and a graphite monochromator at 40 kV and 15 mA. Random powder samples were scanned with a step size of 0.05° 2 theta and a counting time of 1 s per step over a measuring range of 2° to 70° 2 theta. For qualitative analysis, the Rigaku PDXL2 software was used for phase identification based on the ICDD database. For the quantitative analysis of the samples, the diffraction patterns were processed using Siroquant V4 software, and the modal contents were determined by the Rietveld method. Analyses were performed at IGGR RCAES HUN-REN, Budapest, Hungary.

### 2.2.3. FTIR

Fourier transform infrared (FTIR) spectrometry was used for in situ micromineralization and organic material identification on 5 thin sections (172 spectra) using a Bruker FTIR VERTEX 70 instrument equipped with a Bruker HYPERION 2000 microscope with a 20 $\times$  ATR objective and an MCT-A detector. During attenuated total reflectance Fourier transform infrared (ATR) spectroscopy, the samples were contacted with a Ge crystal (0.5 micron) tip under 1 N pressure. The measurement was conducted for 32 s in the 600–4000 cm<sup>−1</sup> range with 4 cm<sup>−1</sup> resolution. Opus 5.5 software was used to evaluate the data. Identification of minerals was based on mineralogical databases (Database of Raman spectroscopy, X-ray diffraction, and chemistry of minerals: <http://rruff.info/> accessed on 1 January 2020) and published references [43–48]. Contamination by epoxy glue and glass was considered. Analyses were performed at IGGR RCAES HUN-REN, Budapest, Hungary.

Polgári and Gyollai [49] summarized the aspects of biogenicity, and complex methodologies were developed on the basis of research experience, high-resolution measurements in situ, and complex interpretations based on structural hierarchy; this approach represents a multitiered verification process for this evidence, as there is no single factor, “microbial biogenicity,” in geological samples [50,51]. Well-founded statements about biogenic origin require a system-based approach and comprehensive, complex, high-resolution studies [52].

#### 2.2.4. SEM–EDS

To determine the elemental composition and distribution of certain sections of the samples, a JEOL JSM-IT700HR electron microscope (20 keV, 3 nA) with an AZtec X-ACT Premium SDD spectrometer was used with a 1–2  $\mu\text{m}$  spatial resolution with a thin graphite cover layer deposited under vacuum. Fifty-three backscattered electron images, 231 spectra, and 8 elemental maps were taken. Analyses were performed at IGGR RCAES HUN-REN, Budapest, Hungary.

### 3. Geological Setting

The Mecsek Mountains, the northernmost unit of the Mecsek Nappe-system, or the Tisza Mega-unit, are considered microplates [53,54] (and were recently situated in the southern part of the Carpathian Basin). The Middle Jurassic began to detach this lithospheric fragment from the southern margin of the European plate. Early Cretaceous volcanic activity and its products were recognized early [55]. The first evidence for intraplate volcanic activity was provided by [56] as peperites from a drill at Kisbattyán (Figure 1C), supporting the interpretation of early researchers [19,20,22]. The radiometric ages are in line with earlier observations and provide evidence that the paroxysm associated with volcanic activity was between 135 and 100 Ma [57].

### 4. Studied Sections

The localities are natural or artificial outcrops, or samples are revealed as loose blocks due to either mining (abandoned ore dump) or agricultural (cultivated plowland) activities situated in the Dezső Rezső Valley and its surrounding plowland. In the latter cases, weathering was not considered a serious overprinting factor because mining ceased in 1956 and the cultivation of plowland that produced samples from agricultural fields has recently progressed.

#### 4.1. Dezső Rezső Valley Outcrops

This valley traverses the continuous Upper Jurassic–Lower Cretaceous sequence from the SE to the NW, including the depositional iron ore bed. On the southern flank of the valley, there are still the remains of uncovered airshafts and scattered blocks from mining. Loose blocks were also collected here (Figures 2–4).

##### 4.1.1. Hydrothermal Deposits (Figures 3 and 4)

These tubular, cylindrical packets of transportation channels were first reported by [30], who considered hydrothermal vent chimneys. These weathered fragments were collected from the valley floor, and both slopes were rarely in situ, more frequently as loose blocks at the SE end of the Dezső Rezső Valley. Hydrothermal deposits are various. Figure 3 shows the remains of the fossilized transport conduits, while Figure 4 highlights the root region of these transport conduits attached to the former sea floor, surrounded by crystallized limestone, holohedral calcite, and sometimes quartz–amethyst crystals.



**Figure 3.** Hydrothermal sediment was collected from the valley floor in 2006. Note the elongated, slender, cylindrical structure of the tubes. The sampling point coordinates are 46.1851° N, 18.4553° E. The scale bar indicates 1 cm.



**Figure 4.** A well-preserved fragment of hydrothermal sediments from its root region (A) collected from the valley floor in 2008. Note the recrystallized lime mud surrounding the conduit channels (B,C). These fluid and gas transporting channels are usually in packets (4–12 channels in a packet) with a diameter between 1 and 4 mm (C). The walls of these materials are not flat but pitted, as if bubbles or drops had imprinted these spherical structures into their walls. (A) Vertical section of the transport conduits in the root region surrounded by calcite crystals. (B) Oblique view of the transport conduits showing the vertical and horizontal sections. (C) Horizontal view and cross-section of the transport conduits. Note the radially grown calcite crystal filaments around the transport conduits nested in the darker-colored micritic matrix. The scale bars indicate 1 cm.

#### 4.1.2. Limestone Beds (Apátvarasd Limestone Fm.)

The outcrop that traverses these beds is an artificial outcrop excavated at the southern slope of the NW end of the Dezső Rezső Valley, 450 m east of the M6 main road. This is described in detail by [27–29,32,58–60]. This section uncovers the Mecsekjánosi Basalt Fm. (fully altered ankaramite), on which the Apátvarasd Limestone Fm. settled (Figure 5). At other points in the valley, weathered versions of the chilled margins of the pillows and vesicles 1–6 mm in diameter are well observed [32]. On the surface of the volcanite, a red, thin, fossiliferous bed rests concordantly and is partially or fully metasomatized.

The fossiliferous bed yielded very rich megafauna and microfauna [28,32]. Coordinates: 46.1854° N, 18.4530° E.



**Figure 5.** Artificial section from the NW wall of the Dezső Rezső Valley in 2006. The section traverses the Mecsekjánosi Basalt (below) and the Apátvarasd Limestone Formations (upper). Fossiliferous limestone basal beds (indicated in dark purplish-brown thin beds) resting on the fully altered surface of the ankaramite volcanite body. Coordinates: 46.1854° N, 18.4530° E.

#### 4.2. Jeri Plowland (Apátvarasd Limestone, Figure 6)

According to the mining data [18], the Dezső Rezső Valley is placed almost perpendicularly to the dip of the iron ore body, which continues in the southern direction from the valley [18] (p. 189) (Figure 2) beneath the plowland beyond a further 200 m. Occasionally, spring or autumn plowing delivers blocks from the lower soil. In this way, we collected these samples in the field (Figure 6).

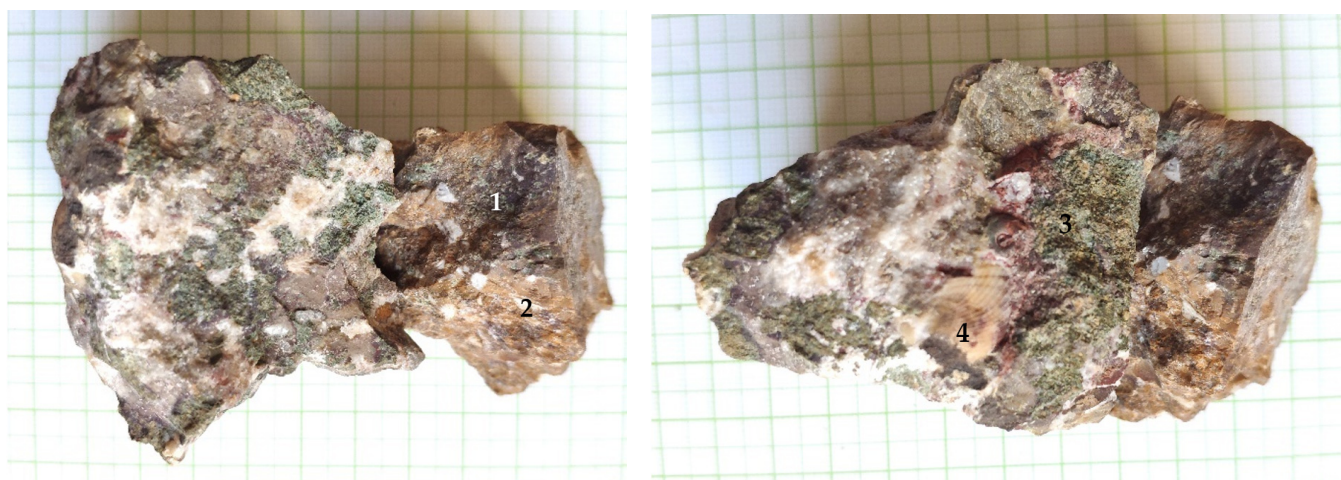


**Figure 6.** Fragment of a peperite block from the Jeri plowland, Zengővárkony, Mecsek Mountains. Note the dark purple-colored mudstone textured micrite (1), the brownish-colored wackestone textured limestone (2), the green-colored volcanite particles (3), and the shelly remaining bivalve (4). Coordinates: 46.1849° N, 18.4533° E. The scale bar indicates 1 cm.

## 5. Results

### 5.1. Textural and Mineralogical Observations

#### Optical Rock Microscopy (OM) and SEM–EDS

In all the thin sections (Figure S1), adequate high-resolution optical rock microscopy (1000×) reveals a series of mineralized microbially produced textures as the main constituents (Figure 7a–c). This microbial microtexture is a basic feature of all samples under transmitted light (Figure S2). Well-preserved and mineralized remains of diverse sequential filaments with pearl necklace-like, vermiform inner signatures, and coccoid-like forms embedded in the samples are observed. The whole sample appears densely woven, often forming opaque parts (Figure 7a). The diameter of the mineralized filaments is approximately 0.5–1 μm, the length of the filaments is variable, and the minerals are very fine-grained (0.5–1 μm). The composition of the brown, opaque part is goethite, which is very fine-grained. It contains traces of Al, Si, P, S, and Ca in different amounts, ranging from a few tenths to some but less than 10 weight percentages. The quartz is segregated. Silica and Fe oxides with Al, Mg, K, and Ca formed Fe-bearing clays. Rare feldspars were detected.

Mineralized cross cuts of hydrothermal discharge channels are characteristic of sample 1 (Figure 7f–h). Cauliflower-like and shell-like stromatolitic structures of quartz and goethite occur. In some shells, there is native sulfur (10 × 50 μm) as well as barite among fine goethite (magnetite?) grains. The shells include feldspar. Rarely, small pyrite (rarely Mn-bearing) grains are preserved. In samples 1 and 4, framboidal-like pseudomorphs occur as goethite, including barite (Figure 8a–h). Samples 4 and 9 contained carbonate matrixes, in which a mineralized microbial network could be observed. Fe-bearing infiltration also occurs with microbial biosignatures (Figure 7d). In sample 9 (peperite), altered glassy tuff occurs as greenish remnants (clay transformation) (Figure 9a). Iron and Ti with V and Mn traces are characteristic of this sample. Sample 12 contains carbonate and Fe-bearing opaque phases. In some parts, breccia-like character occurs, and mineralized microbial biosignatures are characteristic (Figure 9c,d). Decapod crustacean microcoprolite (*Palaxius tetraochetarius* Palik, 1965) occurs in this sample as well as in sample 13, in which crustacean coprolites also contain remnants of mineralized microbial biosignatures (Figure 9c–f). The crustacean decapod microcoprolites contain goethite with the same composition as goethite in the matrix (Figure 9c–e stars). High-resolution SEM–EDS showed the same goethite composition in the mineralized microbially mediated microtexture (Figure 9e,f). All the microcoprolites have similar mineral compositions to those of the carbonate host in which they occur.

In addition, some microfossils (test fragments of benthic foraminifera) occur in sample 13 (Figure 7e). Mineralized microbial biosignatures are also common based on transparent and reflective photos (Figure 10a,b). Elemental maps represent tiny network-like mineralized EPSs with iron and P (and Ti and some Mn) (Figures 9g,h and 10d–h). Rare Ba-bearing Mn oxide grains also occurred. Debris material is not visible.

### 5.2. Mineralogical Composition

#### 5.2.1. X-ray Powder Diffraction

The quantitative mineral compositions of the samples are summarized in Table 2. Quartz, calcite, goethite, hematite, jarosite, siderite, and pyrite were detected.

#### 5.2.2. FTIR

The samples were very fine-grained and fluffy, and debris minerals were not detected. The main Fe minerals are ferrihydrite, goethite, and magnetite. In addition to the ore minerals, quartz, feldspar (albite, orthoclase), ferrierite, phlogopite, celadonite, apatite, calcite, dolomite, rhodochrosite, kutnohorite, and gypsum were detected (Table S1 and Figure S3). The samples are rich in organic matter. SEM–EDS analyses revealed native sulfur, barite, ilmenite, anatase, Ba-bearing Mn oxide, romanèchite (psilomelane), and Fe-bearing clay minerals.

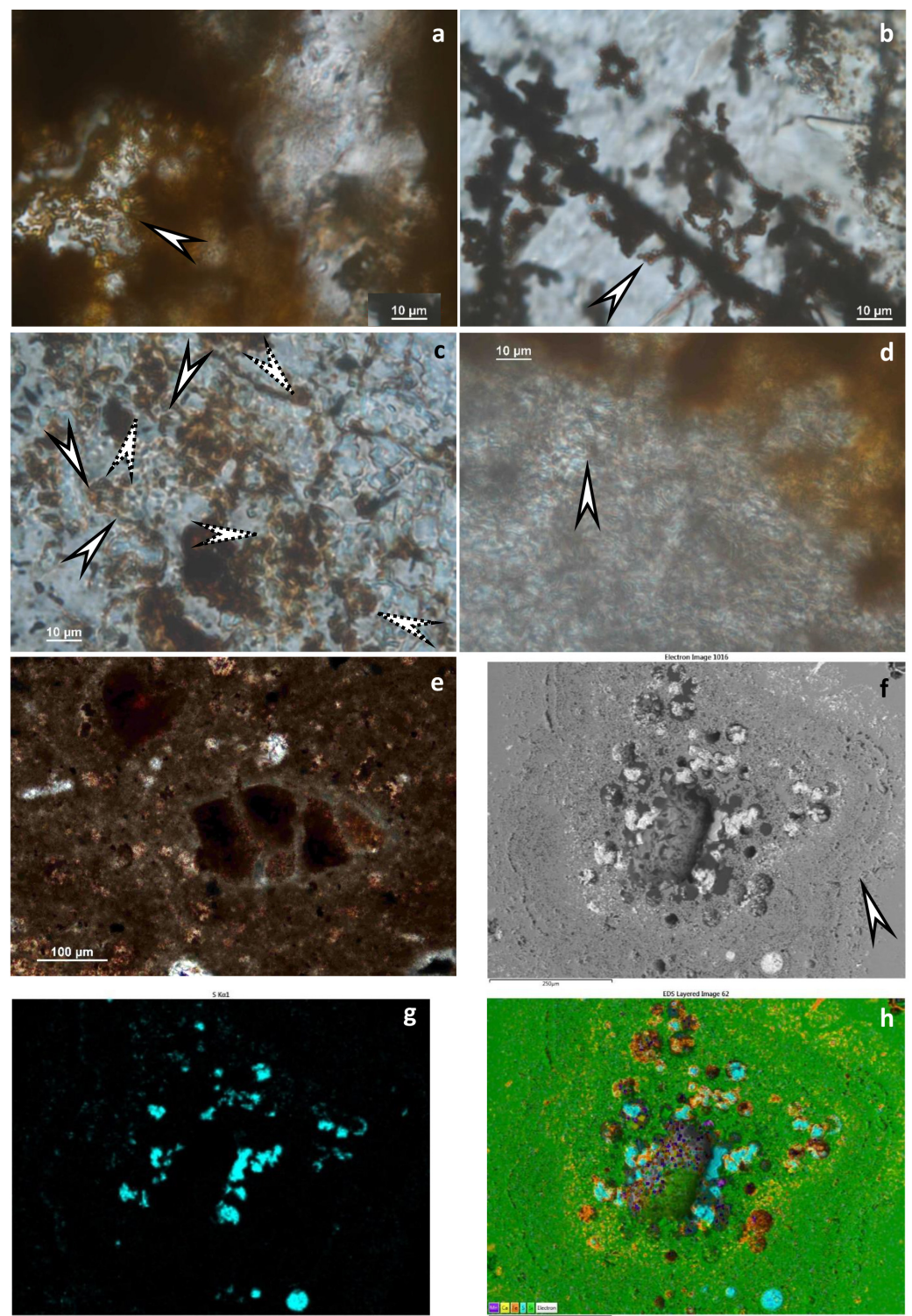


**Figure 7.** Brown, woven goethite-rich mineralized microbial biosignatures are shown by arrows (a–d), on (c) well-preserved and mineralized remains of diverse sequential filaments with pearl necklace-like, vermiform inner signatures are shown by normal arrows, and coccoid-like forms are shown by dashed arrows, transmitted light, 1 Nicol (1 N hereafter), sample 1, 4, 12; (e) Microfossil in a fine-grained clay-rich matrix transmitted light, 1 N, sample 13; (f) Backscattered electron image (BEI hereafter) obtained by SEM–EDS of the stromatolitic structure around the proposed cross cut of the hydrothermal discharge system, sample 1; (g) Native sulfur occurrence in the stromatolitic structure detected on the S elemental map, sample 1; (h) Composed elemental map of (f), color legend from left to right: Mn, Ca, Fe, S, Si.

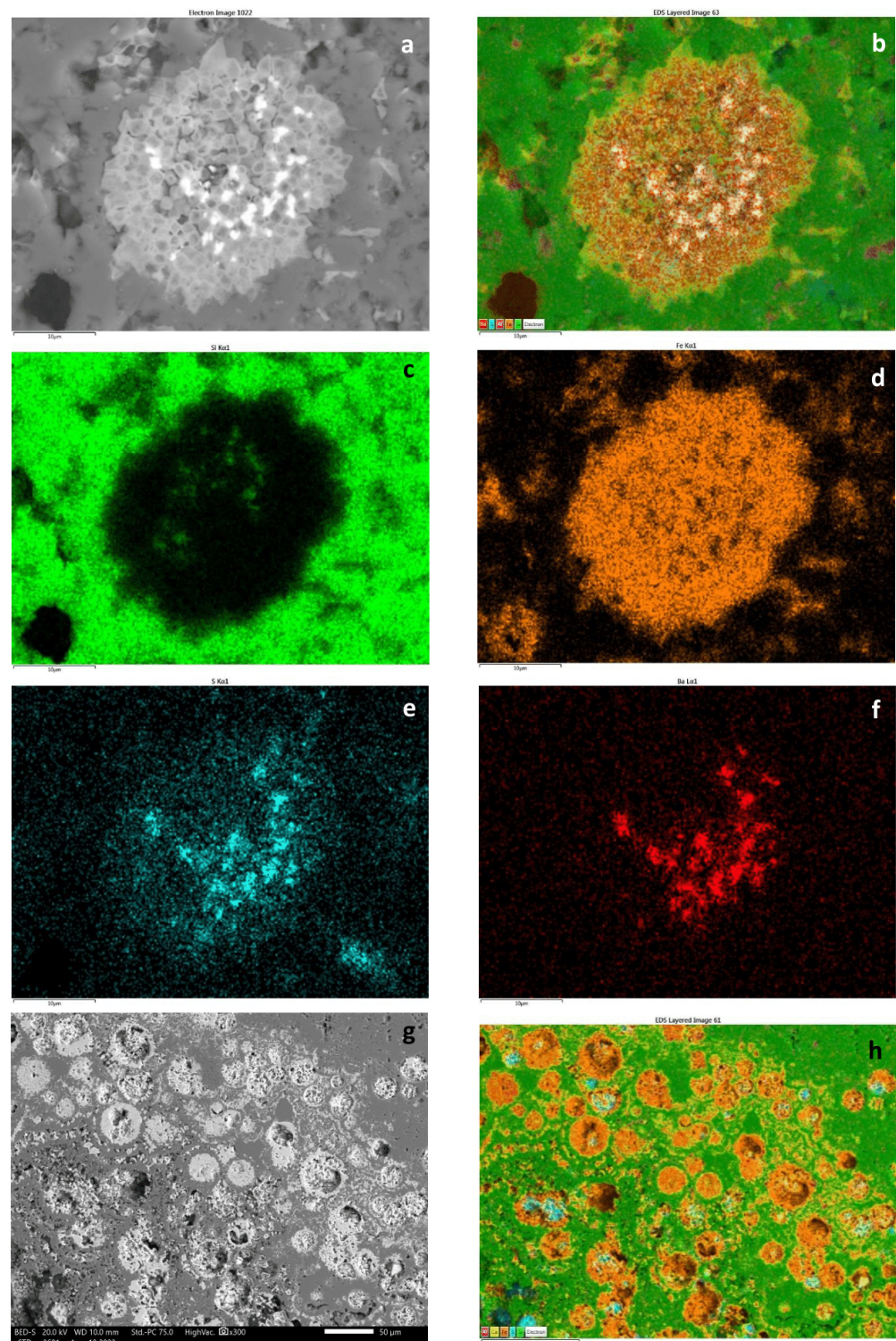


**Figure 8.** Elemental composition of the Fe-rich mineral assemblage and proposed cross-section hydrothermal discharge system. SEM-EDS (BEI), sample 1; (a) Backscattered electron image obtained by SEM-EDS of the Fe-rich mineral assemblage with barite in segregated quartz; morphology of the mineral grains raises previous framboidal Fe-S system, which later oxidizes; (b) Composed elemental map, color legend from left to right: Ba, S, Al, Fe, Si (Al and Si refer to clay minerals); (c–f) Elemental maps of Si, Fe, S, and Ba; (g) Backscattered electron image obtained by SEM-EDS of the proposed Fe-rich cross-cut hydrothermal discharge system in segregated quartz and carbonate host; (h) Composed elemental map, color legend from left to right: Al, Ca, Fe, S, Si (Ca refers to calcite host, Al and Si refer to clay minerals, S refers to native sulfur).

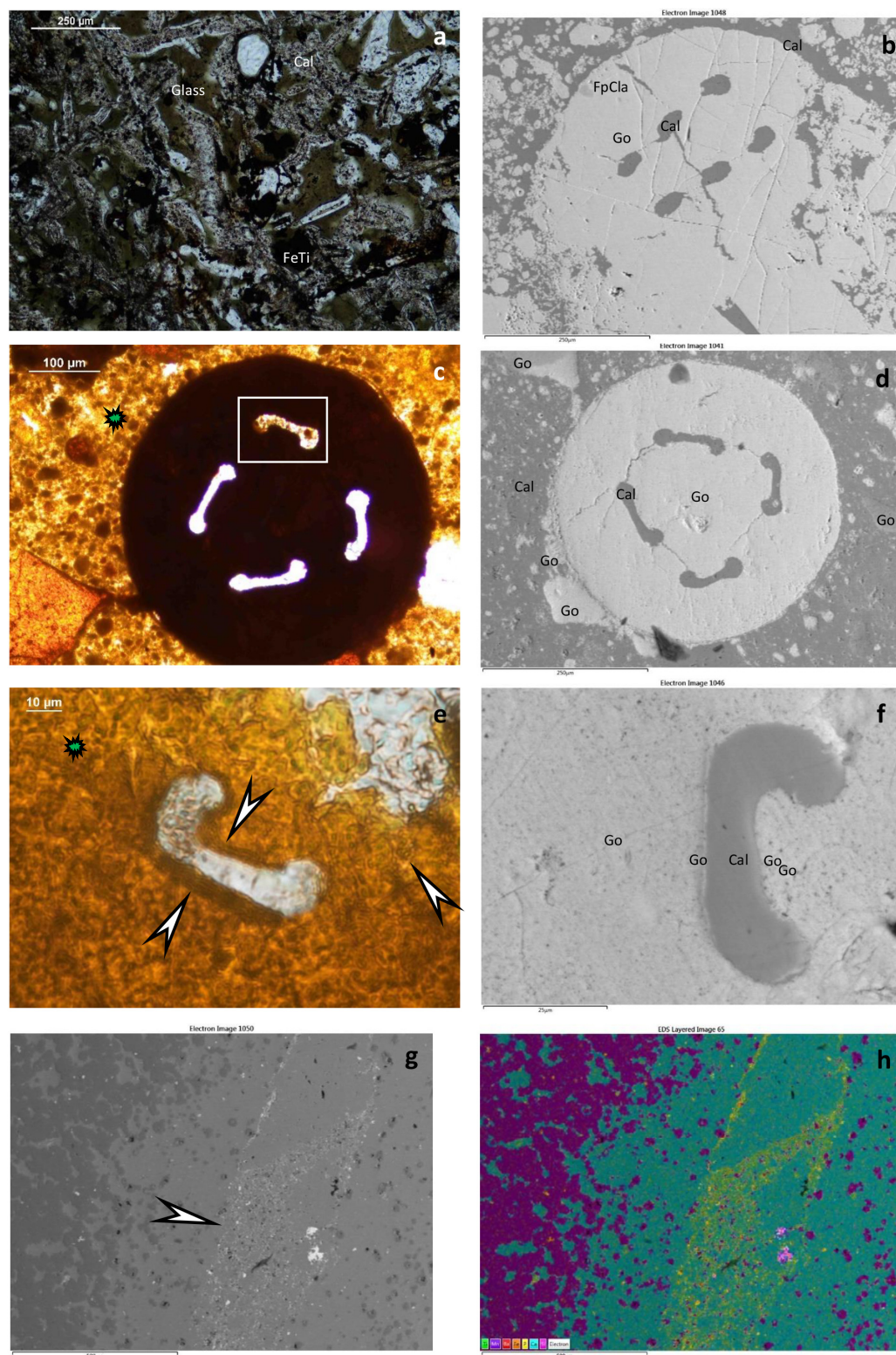


**Figure 9.** Peperite, crustacean microcoprolites, and biomat in merged segregated quartz and carbonate host. (a) Peperite, including volcanic glass (Glass), calcitized altering glass (Cal), and Fe-Ti opaque minerals; transmitted light, 1 N; sample 9; (b) crustacean microcoprolite *Favreina hexaochetarius* Palik, 1965, BEI by SEM-EDS; sample 13, legend: Go-goethite; Cal-calcite; FpCla-feldspar-clay mineral; (c) Goethite-bearing microcoprolite *Palaxius tetraochetarius* Palik, 1965, transmitted light, 1 N; sample 12; (d) Image of *Palaxius tetraochetarius* Palik, 1965 (c), BEI by SEM-EDS, legend: Go-goethite;

Cal-calcite; (d) Enlarged ventral channel of *P. tetraochetarius*; and (c) with brown, woven goethite-rich mineralized microbial biosignatures shown by arrows, transmitted light, 1 N, sample 12. All the microcoprolites have similar mineral compositions to those of the carbonate host in which they occur. As shown in (c,e), the host material is similar to the coprolite material in terms of microtexture (mineralized microbially produced texture, filamentous with sequestered inner forms), mineral composition, and elemental composition, as are the trace elements in goethite (S and P); (f) BEI determined by SEM–EDS (e), legend: Go-goethite; Cal-calcite; (g) Biomat in merged segregated quartz and carbonate host, BEI by SEM–EDS, sample 13; (h) Composed elemental map of (g), color legend from left to right: Ti, Mn, Ba, Fe, P, Ca, Si (P yellow, and Ti, Mn, Fe refer to biomat).

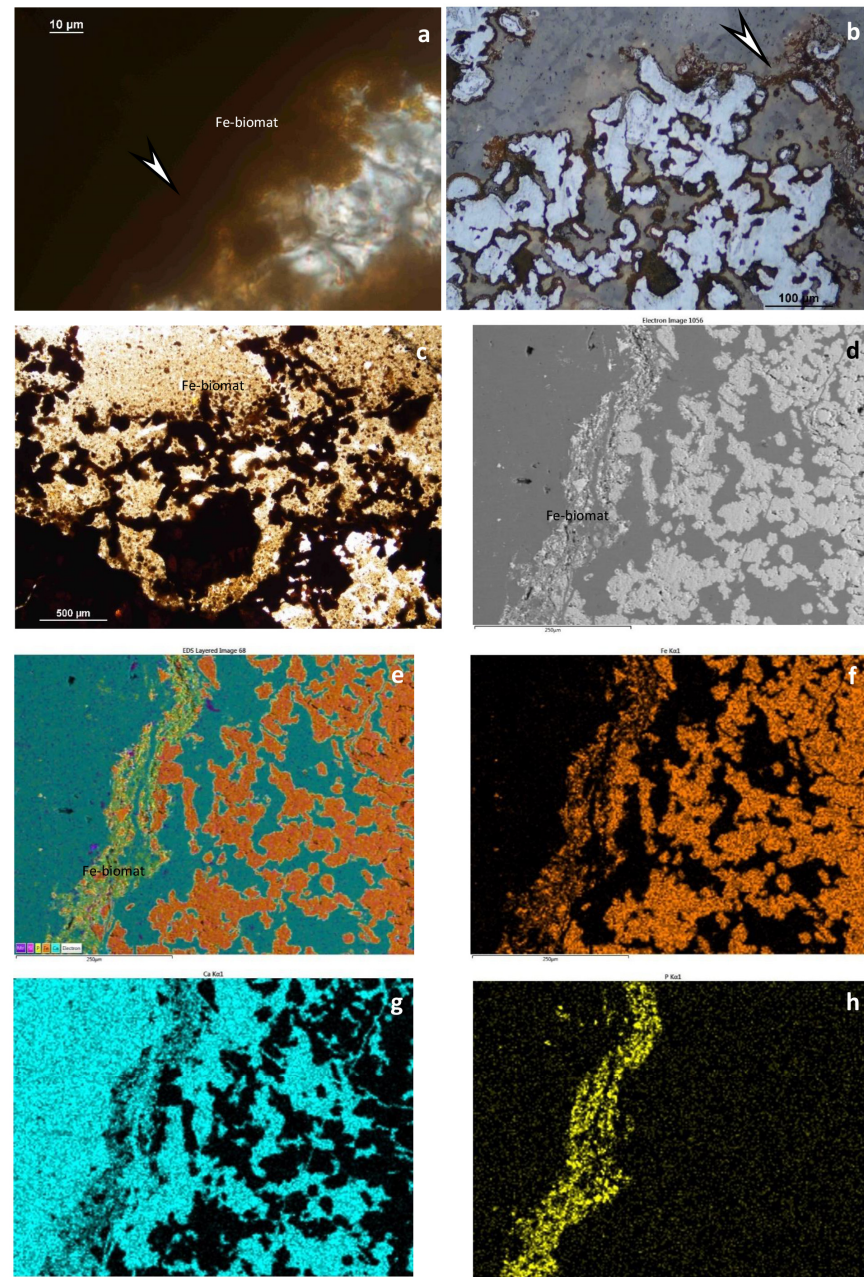


**Figure 10.** Fe-bearing biomat system in segregated quartz and carbonate host. (a) Stromatolitic Fe-bearing biomat (arrow), transmitted light, 1 N, sample 12; (b–d) similar parts of biomat system according to the reflected light image (arrow) (b), transmitted light, 1 N image (c) and BEI obtained via SEM–EDS (d); (e) Composed elemental map of (d), color legend from left to right: Mn, Si, P, Fe, Ca (P, Mn, Fe refers to biomat); (f–h) Fe, Ca, and P elemental maps obtained via SEM–EDS.

**Table 2.** Quantitative mineral compositions of the selected samples determined via XRD. For sample number descriptions, see Table 1.

Sample No.	Calcite	Quartz	Hematite	Goethite	Jarosite	Siderite	Pyrite
1	-	52	-	30	5	-	13
4	2	98	-	-	-	-	-
9	92	7	-	1	-	-	-
12	74	1	2	21	-	2	-
13	67	2	1	30	-	-	-

### 5.3. Microbial Activity

Among the recorded decapod crustacean microcoprolites, the most frequent isp. is *Palaxius tetraochetarius* Palik, 1965 [61], which cooccurs with *Favreina hexaochetarius* Palik, 1965. Figure 9b–f shows this species, with remarkable evidence for the dependence of decapod crustaceans on bacteria. Inside the coprolite (which has excellent preservation) around the paired channels, fine, laminated necklace-like filaments are observed.

### 5.4. Fauna and Food Chain

The Zengővárkony SHV environment provided the most diverse Mesozoic microcoprolite ichnofauna [21,31,59,61], which comprises 11 coprolite species (*Favreina belandoi*, *F. dispentochetarius*, *F. hexaochetarius* (Figure 9b), *F. octoochetarius*, *Helicerina siciliana*, *Parafavreina huaricolcanensis*, *Palaxius darjaensis*, *P. decaochetarius*, *P. salataensis*, *P. tetraochetarius* (Figure 9c,d), and *P. triochetarius* (Figure 9c,d)). With such a diverse microcoprolite fauna, the food supply for these crustaceans became crucial.

Based on the results, the food chain below can be outlined. References to the food chain elements in recent environments are indicated in rounded brackets, and references to the fossil environment at Zengővárkony SHV are indicated in square brackets.

**Primary producers:** vent and symbiotic *bacteria* (as recently noted [37,62]) [this paper].

**Primary consumers** included *crustaceans* (recent counterpart: vent shrimp; [37,63]), [19–21,32,61], *brachiopods* (recent counterpart: vent mussels; [37,64]) [28,29,32,65], and *anthozoans* (recent counterpart: sea anemone; [66]) [67–69].

**First-order carnivores** include *crustaceans* (recent counterparts: decapod crustaceans [37,70]) [as above] and *regular echinoids* (recent counterparts: asteroids, [70]; regular echinoids, [71]) [32,60,72,73].

**Top-order carnivores:** *ammonites* and *belemnites* (recent counterparts: cephalopods, *Vulcanoctopus* [32]; *Benthooctopus* [74]) [27,32].

The scavengers used were *crustaceans* (recent counterpart: blind crabs and fishes, echinoderms, isopods, and amphipods [75]) and *nautilids* (recent counterpart: not known) [32].

## 6. Discussion

### 6.1. Mineralogy

The mineral composition was determined by different methods (XRD, FTIR, and SEM–EDS). The mineral assemblage is summarized in Table 3. According to the XRD results, quartz, calcite, goethite, and pyrite were the main minerals, and traces of hematite, siderite, and jarosite were detected. Jarosite was formed via the oxidation of pyritic ore by microbial mediation [76–78]. This observation and small preserved pyrite grains support sulfidic (pyrite-bearing) proto-mineralization, which was subsequently oxidized to goethite (magnetite?). Goethite contains traces of sulfur, which supports this scenario. Pyrite has Mn traces. Phosphor traces of goethite refer to microbially mediated formation processes. Barite supports sulfide-bearing proto-mineralization, which is subsequently oxidized to goethite and sulfate bonds Ba, forming a few  $\mu\text{m}$  barite grains (Figure 8). The geological background host is carbonate, and the ooze bonds contain some of the metal cations (Fe, Mg, and Mn) in the form of mixed carbonate, double carbonate, and

kutnohorite, as determined by FTIR (Figures 11 and S3). Iron substitution in calcite in samples 12 and 13 is more dominant. Mineralized cross cuts of submarine hydrothermal discharge systems (sedimentary hydrothermal vent systems) with stromatolitic structures built up from quartz and goethite are preserved. In some layers of the stromatolite, native sulfur occurs as the result of microbial sulfide oxidation [79] (Figure 7). Some portion of the sulfate formed barite in the framboidal-like pseudomorphs of goethite (magnetite?). Magnetite is the result of heterotrophic microbial-mediated and partly reduced products of goethite (see [80,81]). Gypsum also supports this scenario, as it is similar to the Úrkút-Csárdahegy occurrence [82].

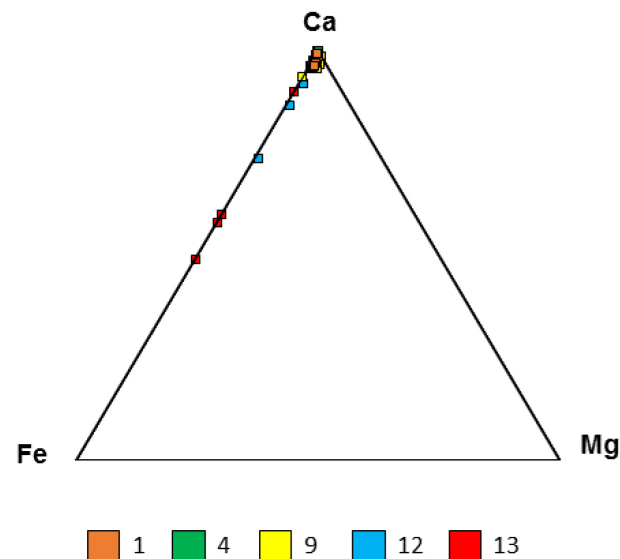


**Figure 11.** Triangle diagram of carbonate composition. The color numbers refer to the samples described in Table 1.

The discharge system offered chemical nutrients for prokaryotic microbes, which provided the basic food chain for this sediment-hosted vent fauna, as [32] discussed in detail, as did the main enrichment process of iron ore formation (indication), which is microbially mediated Fe ore formation [49] (in this sense). The verification must not be limited to only microtextural evidence, although this approach provides robust evidence [83]. Polgári and Gyollai [49] focused their attention on optical rock microscopy photos of the texture of mineralized microbially mediated biosignatures, which offer insight into tiny microtextural forms. Among the compositional evidence, e.g., that mineral ferrihydrite is a microbially mediated Fe oxide-hydroxide, based on natural observations and laboratory experiments. There is also robust mineralogical evidence. Trace elements, such as goethite, also have importance, as they include traces of sulfur, which supports this scenario. Phosphor traces of goethite refer to microbially mediated formation processes [51]. According to the FTIR results, the samples are rich in organic matter. The light sulfur isotope characteristics reported in earlier papers also support this scenario. Microcoprolites from decapod crustaceans accumulate in carbonate ooze. This process is linked to the ecology of that kind of burrow-living decapod: specimens bring their fecal pellets out of the burrows onto the sea floor, from which bottom currents are delivered elsewhere. The composition of the microcoprolites is goethite, which is the same composition as that in the matrix, and it refers to the food for some decapod crustacean species, which consists of microbially mediated Fe oxide and the produced organic matter. The mineralized microbially mediated filamentous microtexture is preserved in the coprolites (Figure 9c–f). Channels were filled with carbonate.

**Table 3.** Mineral assemblages and typical minerals indicative of Eh-pH ranges based on environmental mineralogy. The mineral assemblage compositions were determined via XRD, SEM-EDS, and FTIR spectroscopy analyses. The Eh-pH ranges and microbially mediated mineralogy are based on [49]. Abbreviations. S: syngenetic; D: diagenetic stabilization; EPS: mineral formation on cells and EPS decomposition reservoir.

Minerals/ Processes	Chemical Formula	Eh				pH		Microbially Mediated	S	D	EPS
		Oxic	Suboxic	Anoxic	Acidic	Neutral- Slightly Alkaline	Alkaline				
<i>Native element</i>											
Native sulfur								*	*	*	
<i>Oxides and hydroxides</i>											
Quartz	SiO <sub>2</sub>				*			*		*	
Ferrihydrite	FeOOH		*			*		*	*		
Hematite	Fe <sub>2</sub> O <sub>3</sub>	*	*			*				*	
Goethite	FeOOH	*	*		*		*			*	
Magnetite	Fe <sub>3</sub> O <sub>4</sub>		*	*				*		*	
Anatase	TiO <sub>2</sub> -Fe <sub>x</sub> Ti <sub>(1-x)</sub> O <sub>(2-x)</sub> OH <sub>x</sub>		*			*		*		*	
Ilmenite	FeTiO <sub>3</sub>									*	
Romanèchite psilomelane	[(Ba,H <sub>2</sub> O,Mn <sub>5</sub> O <sub>10</sub> , Ba(Mn <sup>4+</sup> , Mn <sup>3+</sup> )O <sub>10</sub> ·1.4H <sub>2</sub> O)]			*	*		*			*	
<i>Carbonates</i>											
Calcite	Ca (CO <sub>3</sub> )								*		
Dolomite	CaMg(CO <sub>3</sub> ) <sub>2</sub>		*			*		*	*	*	
Rhodochrosite	MnCO <sub>3</sub>		*			*		*		*	
Kutnohorite	(Ca,Mn)(CO <sub>3</sub> ) <sub>2</sub>		*							*	
Siderite	FeCO <sub>3</sub>		*			*		*		*	
<i>Sulphides</i>											
Pyrite	FeS <sub>2</sub>			*	*			*	*	*	
<i>Silicates</i>											
Albite (feldspar)	NaAlSi <sub>3</sub> O <sub>8</sub>					*				*	
Orthoclase (feldspar)	KAlSi <sub>3</sub> O <sub>8</sub>					*				*	
Ferrierite (zeolite)	[Mg <sub>2</sub> (K,Na) <sub>2</sub> Ca <sub>0.5</sub> ](Si <sub>29</sub> Al <sub>7</sub> )O <sub>72</sub> ·18H <sub>2</sub> O		*			*			*	*	
Celadonite	KMg <sub>0.8</sub> Fe <sup>2+</sup> <sub>0.2</sub> Fe <sup>3+</sup> <sub>0.9</sub> Al <sub>0.1</sub> Si <sub>4</sub> O <sub>10</sub> (OH) <sub>2</sub>		*			*		*		*	
Phlogopyte	KMg <sub>3</sub> AlSi <sub>3</sub> O <sub>10</sub> (F,OH) <sub>2</sub> (Fe substitution)									*	
<i>Phosphates</i>											
Apatite	[(Ca <sub>10</sub> (PO <sub>4</sub> ) <sub>6</sub> (OH, F, Cl) <sub>2</sub> )]		*			*	*	*		*	
<i>Sulfates</i>											
Barite	Ba(SO <sub>4</sub> )	*				*		*	*	*	
Gypsum	CaSO <sub>4</sub> ·2H <sub>2</sub> O		*		*			*	*	*	
Jarosite	Fe <sup>3+</sup> <sub>3</sub> (SO <sub>4</sub> ) <sub>2</sub> (OH) <sub>6</sub>			*	*			*	*	*	
Organic material								*	*		

\* This means that the given mineral occurs under those conditions.

Quartz occurs as a segregated mineral. As ferrihydrite was determined by FTIR, its stabilization to goethite is accompanied by quartz segregation [84,85]. Al, Mg, K, and Ca with silica formed feldspar, zeolite (ferrierite), and Fe-bearing clay minerals (via SEM-EDS). These elements represent the decomposition of cell and EPS material, which is subsequently mineralized [49,51].

Tiny structures of mineralized cells and extracellular polymeric substances (EPSs) are clearly visible on SEM–EDS elemental maps, and the substances are composed of Fe, P, some Mn traces, and Ti. These are mineralized Fe biomaterials (Figures 7a–d, 9g,h and 10a–h). Rarely small apatite grains follow the biomat network. Sample 9 is peperite, which contains altered volcanic glass, Fe-bearing clay minerals, and Fe–Ti grains (ilmenite and anatase).

The mineral assemblage (ferrihydrite) and filamentous microbially mediated microtexture refer to suboxic, semineutral conditions during vent formation, which support the activity of Fe-oxidizing microbes on sulfidic precursor materials, which are common in hydrothermal systems. Trace amounts of Mn oxide indicate locally more oxidized conditions.

#### 6.2. Bacteria–Crustacean Interactions

On the one hand, all the conclusions drawn here do not support recent observations because the available observations on the physiology of recent decapod crustaceans are limited and because there are no known host decapod species that produce microcoprolites with filament structures, as described herein. On the other hand, as Felgenhauer [40] noted, the evolution of the digestive tract of decapod crustaceans is considerably conserved; therefore, limited research may be needed.

The typical internal channel system of the coprolites of decapod crustaceans is produced by the whole gastric tract of decapods. The channels are formed in the pyloric sac (foregut) [40], and fecal compaction occurs in the midgut [86]. The duration of digestion from the foregut through the hindgut varies from 30 min in small copepods to more than 150 h in larger lobsters [86], providing the necessary duration for supposed internal bacteria to grow inside the gut and grow over the internal channels of the microcoprolite before emptying. Bacteria live on decapods; hence, they even densely cover the cuticle of hydrothermal vent decapod crustacean antennae [87], but even inside decapod crustaceans, bacterial communities exist. Zbinden and Cambon-Bonavita [88] reported internal symbioses between bacteria and decapod crustaceans on the internal surface of the decapod gut. This finding provides a third explanation for the laminated bacterial filaments deposited on the internal channel walls of the microcoprolites: bacteria incorporated the internal channels even inside the gut of the host animal. However, in our patient, who had only fossilized microcoprolites but not fossilized decapod tissue, this could not be resolved or answered with high certainty. Finally, based on recent observations [88,89], it seems plausible that the bacteria-like filaments on the internal channel walls of microcoprolites are directly linked to their food and/or gut epibiont bacteria on the epithelium [90].

#### 6.3. Minerals–Crustacean Interactions

Our mineralogical observations are in line with the observations on the gut contents of recent vent-related crustaceans. Zbinden and Cambon-Bonavita [88] (Figure 7a,b) presented a semithin section of the midgut of *Rimicaris exoculata* from a MAR locality that showed black and brown mineral particles (iron sulfides and oxides, respectively); however, this biological research did not focus on the spatial characteristics of the gut content or the spatial analysis of the excreta of their host. The crustacean decapod microcoprolites contain goethite in our case, which is a convincing correlation between the fossil and recent decapod crustacean gut contents.

#### 6.4. Ecology

In the ecological buildup of the Zengővárkony SHV compared with its recent counterparts, the greatest difference is the complete lack of bivalves, although even in the fossil record, bivalves are reported from deep marine hydrothermal vents. However, this approach becomes reasonable if one takes into consideration the Mesozoic marine revolution [91], which swept brachiopods from the original ecotopes and opened the path to bivalves that currently play a significant role in all marine ecosystems, including hydrothermal vents. The fossil ecosystem of the Zengővárkony SHV hosted a rich, partly endemic

community reconstructed from the base producers to the top consumers as complex and vividly 135 Ma before their recent counterparts.

## 7. Conclusions

Detailed microtextural and mineralogical analysis of selected samples from the Early Cretaceous Zengővárkony (Mecsek Mountains, Tisza microplate, Hungary) SHV provided evidence for microbial activity at this shallow marine hydrothermal vent site. This is in intimate connection with the rich and diverse decapod crustacean megafauna. Filamental bacteria formed and grew into coprolite channels, and diffuse bacteria and extracoprolitic bacterial mats also reveal the bacterial activity and its presence in this SHV environment. It provided the primary food source for this vivid, diverse, and partly endemic fossil environment. Based on this research, a complete food web for a shallow marine fossil hydrothermal vent site is established. Fossil counterparts for the elements of recent hydrothermal vent ecosystems are also proposed.

Recent observations of living decapod crustaceans at MAR hydrothermal vents revealed that crustaceans feed on iron sulfide and iron oxide particles that pass through their digestive tracts. The sizes of these particles vary between 0.5 and 15  $\mu\text{m}$ , and the particles go through the digestive tract. The material of decapod crustacean microcoprolites is goethite at the Zengővárkony SHV, which implies that crustaceans fed on the bacterial mats collected these mineral particles and sometimes emptied later.

This complex ecological and mineralogical analysis provided direct evidence for the presence of bacteria in fossil SHV environments on the one hand and the intimate connection between bacteria and decapod crustaceans in hydrothermal environments 135 Ma before. Further research to determine the complex relationship between decapod crustaceans and vent-related bacteria seems to be more complex than previously thought based on recent observations of living decapods in MAR environments. We conclude that similar fossil environments are considered useful indicators of the initial marine intraplate rifting that produced unique carbonate sediment-hosted environments. Therefore, fossil carbonate SHV environments are indicators of active plate margins in the geological past.

**Supplementary Materials:** The following supporting information can be downloaded at: <https://www.mdpi.com/article/10.3390/min14020125/s1>, Figure S1. Samples and thin sections of samples; Figure S2. Optical rock microscopy photos; Figure S3. Representative FTIR measurements on sample 1; Table S1. Mineralogy and organic compounds by Infra-red spectroscopy (FTIR).

**Author Contributions:** L.B. and M.P. contributed to the study's conception and design. Field work was performed by L.B. Material preparation, data collection, and analysis were performed by M.P. Instrumental measures, analysis, and interpretation were performed by I.G., M.S. and I.K. The first draft of the manuscript was written by the authors, and all the authors commented on previous versions of the manuscript. All authors have read and agreed to the published version of the manuscript.

**Funding:** Partial financial support was received from LB via a Bólyai János Research Grant for Field Work (Grant number BO414/10) between 2010 and 2013; Osztrák-Magyar Akció Alapítvány (Grant number: 99öu02) financed the sulfur stable isotope measurements.

**Data Availability Statement:** Dataset is provided in the Supplementary Material.

**Acknowledgments:** The authors are thankful to Magali Zbinden (Sorbonne Université Equipe Adaptations aux Milieux Extrêmes, Paris, France) for the discussion on the ecology of recent decapod crustaceans of from hydrothermal vents.

**Conflicts of Interest:** The authors declare no competing interests.

## References

1. Corliss, J.B.; Dymond, J.; Gordon, L.I.; Edmond, J.M.; Von Herzen, R.P.; Ballard, R.D.; Green, K.; Williams, D.; Bainbridge, A.; Crane, K.; et al. Submarine thermal springs on the Galápagos Rift. *Science* **1979**, *203*, 1073–1083. [CrossRef]
2. Haymon, R.M.; Koski, R.A.; Sinclair, C. Fossils of hydrothermal vent worms from Cretaceous sulfide ores of the Samail Ophiolite, Oman. *Science* **1984**, *223*, 1407–1409. [CrossRef]
3. Ramondenc, P.; Germanovich, L.N.; Von Damm, K.L.; Lowell, R.P. The first measurements of hydrothermal heat output at 9°50'N, East Pacific Rise. *Earth Planet. Sci. Lett.* **2006**, *245*, 487–497. [CrossRef]
4. Beaulieu, S.E.; Szafranski, K.M. InterRidge Global Database of Active Submarine Hydrothermal Vent Fields Version 3.4. PANGAEA. 2020. Available online: <https://doi.pangaea.de/10.1594/PANGAEA.917894> (accessed on 1 January 2022).
5. Georgieva, M.N.; Little, C.T.S.; Maslennikov, V.V.; Glover, A.G.; Ayupova, N.R.; Herrington, R.J. The history of life at hydrothermal vents. *Earth-Sci. Rev.* **2021**, *217*, 103602. [CrossRef]
6. Bemis, K.; Lowell, R.P.; Farough, A. Diffuse flow on and around hydrothermal vents at mid-ocean ridges. *Oceanography* **2012**, *25*, 182–191. [CrossRef]
7. Price, R.E.; Giovannelli, D. A Review of the geochemistry and microbiology of marine shallow-water hydrothermal vents. In *Reference Module in Earth Systems and Environmental Sciences*; Elsevier: Amsterdam, The Netherlands, 2017. [CrossRef]
8. Procesi, M.; Ciotoli, G.; Mazzini, A.; Etiope, G. Sediment-hosted geothermal systems: Review and first global mapping. *Earth-Sci. Rev.* **2019**, *192*, 529–544. [CrossRef]
9. Bell, J.B.; Woulds, C.; Brown, L.E.; Sweeting, C.J.; Reid, W.D.K.; Little, C.T.S.; Glover, A.G. Macrofaunal ecology of sedimented hydrothermal vents in the Bransfield Strait, Antarctica. *Front. Mar. Sci.* **2016**, *3*, 32. [CrossRef]
10. Kamenev, G.M.; Fadeev, V.I.; Selin, N.I.; Tarasov, V.G. Composition and distribution of macro- and meiobenthos around sublittoral hydrothermal vents in the Bay of Plenty, New Zealand. *N. Z. J. Mar. Freshw. Res.* **1993**, *27*, 407–418. [CrossRef]
11. Levin, L.A.; Mendoza, G.F.; Konotchick, T.; Lee, R. Macrobenthos community structure and trophic relationships within active and inactive Pacific hydrothermal sediments. *Deep. Sea Res. Part II Top. Stud. Oceanogr.* **2009**, *56*, 1632–1648. [CrossRef]
12. Bernardino, A.F.; Levin, L.A.; Thurber, A.R.; Smith, C.R. Comparative composition, diversity and trophic ecology of sediment macrofauna at vents, seeps and organic falls. *PLoS ONE* **2012**, *7*, e33515. [CrossRef]
13. Campbell, K.A. Hydrocarbon seep and hydrothermal vent paleoenvironments and paleontology: Past developments and future research directions. *Palaeogeogr. Palaeoclim. Palaeoecol.* **2006**, *232*, 362–407. [CrossRef]
14. Sievert, S.M.; Hügl, M.; Taylor, C.D.; Wirsén, C.O. Sulfur oxidation at deep-sea hydrothermal vents. In *Microbial Sulfur Metabolism*; Dahl, C., Friedrich, C.G., Eds.; Springer: Berlin/Heidelberg, Germany, 2008; pp. 238–258. [CrossRef]
15. Wirsén, C.O.; Brinkhoff, T.; Kuever, J.; Muyzer, G.; Molyneux, S.; Jannasch, H.W. Comparison of a new *Thiomicrospira* strain from the Mid-Atlantic Ridge with known hydrothermal vent isolates. *Appl. Environ. Microbiol.* **1998**, *64*, 4057–4059. [CrossRef] [PubMed]
16. Detmers, J.; Brüchert, V.; Habicht, K.S.; Kuever, J. Diversity of sulfur isotope fractionations by sulfate-reducing prokaryotes. *Appl. Environ. Microbiol.* **2001**, *67*, 888–894. [CrossRef]
17. Pellerin, A.; Antler, G.; Holm, S.A.; Findlay, A.J.; Crockford, P.W.; Turchyn, A.W.; Jørgensen, B.B.; Finster, K. Large sulfur isotope fractionation by bacterial sulfide oxidation. *Sci. Adv.* **2019**, *5*, eaaw1480. [CrossRef] [PubMed]
18. Molnár, J. A zengővárkonyi vasércutatás. *Bányászati Lapok* **1961**, *94*, 187–194.
19. Sztrókay, K.I. Mecseki vasércképződés. *Magy. Tud. Akad. Műszaki Oszt. Közl.* **1952**, *3*, 11–23.
20. Pantó, G.; Varrók, K.; Kopek, G. Nouvelles contributions à la géologie du gisement de minerai de fer de Zengővárkony. *Földtani Közlöny* **1955**, *85*, 125–144.
21. Palik, P. Remains of crustacean excrement from the Lower Cretaceous of Hungary. *Micropaleontology* **1965**, *11*, 98–104. [CrossRef]
22. Pantó, G. Mezozoós magmatizmus Magyarországon. *Magy. Áll. Földt. Int. Évkönyve* **1961**, *49*, 785–799.
23. Hetényi, R.; Hámor, G.; Nagy, I. *Magyarászó a Mecsek Hegység Földtani Térképéhez, 10,000-es Sorozat*; Geological Institute of Hungary: Budapest, Hungary, 1968.
24. Császár, G. Urgonian facies of the Tisza Unit. *Acta Geol. Hung.* **1992**, *35*, 263–285.
25. Császár, G. Urgon Formations in Hungary with special reference to the Eastern Alps, the Western Carpathians and the Apuseni Mountains. *Geol. Hung. Ser. Geol.* **2002**, *25*, 1–209.
26. Bércziné, M.A.; Császár, G.; Nusszer, A. Stratigraphy and geological evolution of the Mesozoic basement of the Mecsek Zone in the Central Part of the Great Hungarian Plain (East-Central Hungary). *Földtani Közlöny* **1996**, *126*, 185–207.
27. Bujtor, L.; Janssen, N.M.; Verreussel, R.M. Early Cretaceous (Valanginian and Hauterivian) belemnites and organic-walled dinoflagellate cysts from a marine hydrothermal vent site and adjacent facies of the Mecsek Mts., Hungary. *Neues Jahrb. Geol. Paläontologie* **2013**, *269*, 135–148. [CrossRef]
28. László, B. Early Valanginian brachiopods from the Mecsek Mts. (southern Hungary) and their palaeobiogeographical significance. *Neues Jahrb. Geol. Paläontologie Abh.* **2006**, *241*, 111–152. [CrossRef]
29. Bujtor, L. A unique Valanginian paleoenvironment at an iron ore deposit near Zengővárkony (Mecsek Mts, South Hungary), and a possible genetic model. *Cent. Eur. Geol.* **2007**, *50*, 183–198. [CrossRef]
30. Jáger, V.; Molnár, F. Lower Cretaceous continental rift-type black smoker system in the East Mecsek Mts. *Mitteil. Österr. Mineralog. Ges.* **2009**, *155*, 70.

31. Jäger, V.; Molnár, F.; Buchs, D.; Koděra, P. The connection between iron ore formations and “mud-shrimp” colonizations around sunken wood debris and hydrothermal sediments in a Lower Cretaceous continental rift basin, Mecsek Mts., Hungary. *Earth-Sci. Rev.* **2012**, *114*, 250–278. [[CrossRef](#)]
32. Bujtor, L.; Nagy, J. Fauna, palaeoecology and ecotypes of the Early Cretaceous sediment hosted hydrothermal vent environment of Zengővárkony (Mecsek Mountains, Hungary). *Palaeogeogr. Palaeoclim. Palaeoecol.* **2021**, *564*, 110179. [[CrossRef](#)]
33. Beaulieu, S.E.; Baker, E.T.; German, C.R.; Maffei, A. An authoritative global database for active submarine hydrothermal vent fields. *Geochem. Geophys. Geosyst.* **2013**, *14*, 4892–4905. [[CrossRef](#)]
34. Cohen, K.; Finney, S.; Gibbard, P.; Fan, J.-X. The ICS International Chronostratigraphic Chart. *Episodes* **2013**, *36*, 199–204. [[CrossRef](#)]
35. Ferretti, A.; Messori, F.; Di Bella, M.; Sabatino, G.; Quartieri, S.; Cavalazzi, B.; Italiano, F.; Barbieri, R. Armoured sponge spicules from Panarea Island (Italy): Implications for their fossil preservation. *Palaeogeogr. Palaeoclim. Palaeoecol.* **2019**, *536*, 109379. [[CrossRef](#)]
36. Di Bella, M.; Sabatino, G.; Quartieri, S.; Ferretti, A.; Cavalazzi, B.; Barbieri, R.; Foucher, F.; Messori, F.; Italiano, F. Modern Iron Ooids of Hydrothermal Origin as a Proxy for Ancient Deposits. *Sci. Rep.* **2019**, *9*, 7107. [[CrossRef](#)] [[PubMed](#)]
37. Van Dover, C.L. *The Ecology of Deep-Sea Hydrothermal Vents*; Princeton University: Press, Princeton, NJ, USA, 2000.
38. Sievert, S.M.; Brinkhoff, T.; Muyzer, G.; Ziebis, W.; Kuever, J. Spatial heterogeneity of bacterial populations along an environmental gradient at a shallow submarine hydrothermal vent near Milos Island (Greece). *Appl. Environ. Microbiol.* **1999**, *65*, 3834–3842. [[CrossRef](#)]
39. Pohl, M.E. Ecological observations on *Callianassa major* Say at Beaufort, North Carolina. *Ecology* **1946**, *27*, 71–80. [[CrossRef](#)]
40. Felgenhauer, B.E. Internal anatomy of the Decapoda: An overview. In *Microscopic Anatomy of Invertebrates, Decapod Crustacea*; Harrison, F.W., Humes, A.G., Eds.; Wiley-Liss Inc.: New York, NY, USA, 1992; Volume 10, pp. 45–75.
41. Schweigert, G.; Seegis, D.B.; Fels, A.; Leinfelder, R.R. New internally structured decapod microcoprolites from Germany (Late Triassic/Early Miocene), Southern Spain (Early/Middle Jurassic) and Portugal (Late Jurassic): Taxonomy, paleoecology, and evolutionary implications. *Pal. Zeitschr.* **1997**, *71*, 51–69. [[CrossRef](#)]
42. Aliani, S.; Bianchi, N.C.; Cocito, S.; Dando, P.R.; Meloni, R.; Morri, C.; NieMeyer, A.; Peirano, A.; Ziebis, W. A map of seagrass meadows in Paleochori Bay (Milos Island, Greece), a marine area with hydrothermal activity. *Rapp. Comm. Int. Mer. Médit.* **1998**, *35*, 512–513.
43. Madejová, J. Baseline studies of the clay minerals society source clays: Infrared methods. *Clays Clay Miner.* **2001**, *49*, 410–432. [[CrossRef](#)]
44. Parikh, S.J.; Chorover, J. ATR-FTIR spectroscopy reveals bond formation during bacterial adhesion to iron oxide. *Langmuir* **2006**, *22*, 8492–8500. [[CrossRef](#)]
45. Glotch, T.D.; Rossman, G.R. Mid-infrared reflectance spectra and optical constants of six iron oxide/oxyhydroxide phases. *Icarus* **2009**, *204*, 663–671. [[CrossRef](#)]
46. Beasley, M.M.; Bartelink, E.J.; Taylor, L.; Miller, R.M. Comparison of transmission FTIR, ATR, and DRIFT spectra: Implications for assessment of bone bioapatite diagenesis. *J. Archaeol. Sci.* **2014**, *46*, 16–22. [[CrossRef](#)]
47. Müller, C.M.; Pejčić, B.; Esteban, L.; Piane, C.D.; Raven, M.; Mizaikoff, B. Infrared Attenuated Total Reflectance Spectroscopy: An Innovative Strategy for Analyzing Mineral Components in Energy Relevant Systems. *Sci. Rep.* **2014**, *4*, 6764. [[CrossRef](#)] [[PubMed](#)]
48. Zviagina, B.B.; Drits, V.A.; Dorzhieva, O.V. Distinguishing Features and Identification Criteria for K-Dioctahedral 1M Micaceous (Illite-Aluminoceladonite and Illite-Glauconite-Celadonite Series) from Middle-Infrared Spectroscopy Data. *Minerals* **2020**, *10*, 153. [[CrossRef](#)]
49. Polgári, M.; Gyollai, I. Comparative study of formation conditions of Fe-Mn Ore Microbialites based on mineral assemblages: A critical self-overview. *Minerals* **2022**, *12*, 1273. [[CrossRef](#)]
50. Cady, S.L.; Farmer, J.D.; Grotzinger, J.P.; Schopf, J.W.; Steele, A. Morphological Biosignatures and the Search for Life on Mars. *Astrobiology* **2003**, *3*, 351–369. [[CrossRef](#)] [[PubMed](#)]
51. Polgári, M.; Gyollai, I.; Fintor, K.; Horváth, H.; Pál-Molnár, E.; Biondi, J.C. Microbially Mediated ore-forming processes and cell mineralization. *Front. Microbiol.* **2019**, *10*, 2731. [[CrossRef](#)]
52. Knoll, A.H.; Canfield, D.E.; Konhauser, K.O. *Fundamentals of Geobiology*; Wiley-Blackwell: Oxford, UK, 2012; p. 456.
53. Csontos, L.; Vörös, A. Mesozoic plate tectonic reconstruction of the Carpathian region. *Palaeogeogr. Palaeoclim. Palaeoecol.* **2004**, *210*, 1–56. [[CrossRef](#)]
54. Haas, J.; Péró, C. Mesozoic evolution of the Tisza Mega-unit. *Int. J. Earth Sci.* **2004**, *93*, 297–313. [[CrossRef](#)]
55. Hofmann, K. A Vihorlat-Guttin-hegység némely quarctartalmu trachytjának plagioklas-kristályairól (1873). In *Hungarian Geological Bulletin (Földtani Közlemény)*; Geological Institute of Hungary: Budapest, Hungary, 1873; p. 100. (In Hungarian)
56. Viczián, I. Submarine ausbruch- und Gesteinsetzungserscheinungen im unterkrätetazischen Diabaskomplex der Bohrung Kisbattyán Nr. 1. *Ann. Rep. Geol. Inst. Hung.* **1966**, *1964*, 75–92.
57. Harangi, S.; Árvai-Soós, G. Early Cretaceous volcanic rocks of the Mecsek Mountains (South Hungary) I. Mineralogy and petrology. *Földtani Közlemény* **1993**, *123*, 129–165.
58. Bujtor, L. The Early Valanginian ammonite, brachiopod and crustacean fauna of the Mecsek Mts. and its relationships with the embryonic shallow water hydrothermal vent at Zengővárkony (Mecsek Mts., South Hungary). *Cretac. Res.* **2011**, *32*, 565–574. [[CrossRef](#)]

59. Bujtor, L. A Valanginian crustacean microcoprolite ichnofauna from the shallow-marine hydrothermal vent site of Zengővárkony (Mecsek Mts., Hungary). *Facies* **2012**, *58*, 249–260. [[CrossRef](#)]
60. Bujtor, L. The paleontological character of the Lower Cretaceous (Valanginian) hydrothermal vent filling of the Mecsek Mts, Hungary. *Földtani Közlemény* **2012**, *142*, 137–148.
61. Bujtor, L.; Szinger, B. Micropaleontological observations on the Lower Cretaceous iron ore-related formations of the Mecsek Mts. (Upper Valanginian–Lower Hauterivian, South Hungary). *Cent. Eur. Geol.* **2018**, *61*, 136–159. [[CrossRef](#)]
62. Lee, W.-K.; Juniper, S.K.; Perez, M.; Ju, S.-J.; Kim, S.-J. Diversity and characterization of bacterial communities of five co-occurring species at a hydrothermal vent on the Tonga Arc. *Ecol. Evol.* **2021**, *11*, 4481–4493. [[CrossRef](#)] [[PubMed](#)]
63. Versteegh, E.A.; Van Dover, C.L.; Van Audenhaege, L.; Coleman, M. Multiple nutritional strategies of hydrothermal vent shrimp (*Rimicaris hybisae*) assemblages at the Mid-Cayman Rise. *Deep. Sea Res. Part I Oceanogr. Res. Pap.* **2023**, *192*, 103915. [[CrossRef](#)]
64. Hessler, R.R.; Smithey, W.M. The distribution and community structure of megafauna at the Galapagos Rift hydrothermal vents. In *Hydrothermal Processes at Seafloor Spreading Centers*; Rona, P.A., Bostrom, K., Laubier, L., Smith, K., Jr., Eds.; Plenum Press: New York, NY, USA, 1984; pp. 735–770.
65. Bujtor, L.; Vörös, A. New kingenoid (Terebratellidina) brachiopods with larger body sizes from the Early Cretaceous of Zengővárkony (Mecsek Mountains, Hungary). *J. Paléontol.* **2019**, *94*, 475–488. [[CrossRef](#)]
66. Fautin, D.G.; Barber, B.R. *Maractis rimicarivora*, a new genus and species of sea anemone (Cnidaria: Anthozoa: Actiniaria: Actinostolidae) from an Atlantic hydrothermal vent. *Proc. Biol. Soc. Wash.* **1999**, *112*, 624–631.
67. Kolosváry, G. Les coralliaires du Crétacé de la Hongrie. *Magy. Áll Földt Int. Évkönyve* **1954**, *42*, 67–163.
68. Kolosváry, G. Über erste Korallenfunde aus der Jura-Zeit des Mecsek-Gebirges in Süd-Ungarn. *Acta Univ. Szeged. Acta Biol.* **1956**, *2*, 199–207.
69. Kolosváry, G. Korallen aus der Unterkreide des Mecsek-Gebirges. *Acta Univ. Szeged. Acta Biol.* **1959**, *5*, 125–128.
70. Voight, V.R. A review of predators and predation at deep-sea hydrothermal vents. *Cah. Biol. Mar.* **2000**, *41*, 155–166.
71. Van Dover, C.L.; Desbruyères, D.; Segonzac, M.; Comtet, T.; Saldanha, L.; Fiala-Médioni, A.; Langmuir, C. Biology of the Lucky Strike hydrothermal field. *Deep. Sea Res. I* **1996**, *43*, 1509–1529. [[CrossRef](#)]
72. Bujtor, L. Cretaceous echinoid (*Plegiocidarid*) from the Mecsek Mts, Hungary. *Földtani Közlemény* **2013**, *143*, 321–326.
73. González, A.F.; Guerra, A.; Pascual, S.; Briand, P. *Vulcanoctopus hydrothermalis* gen. et sp. nov. (Molluska, Cephalopoda): An octopod from a deep-sea hydrothermal vent site. *Cah. Biol. Mar.* **1998**, *39*, 169–184.
74. Strugnell, J.; Voight, J.R.; Collins, P.C.; Allcock, A.L. Molecular phylogenetic analysis of a known and a new hydrothermal vent octopod: Their relationships with the genus *Benthoctopus* (Cephalopoda: Octopodidae). *Zootaxa* **2009**, *2096*, 442–459. [[CrossRef](#)]
75. Kniesz, K.; Jazdzewska, A.M.; Arbizu, P.M.; Kihara, T.C. DNA Barcoding of Scavenging Amphipod Communities at Active and Inactive Hydrothermal Vents in the Indian Ocean. *Front. Mar. Sci.* **2022**, *8*, 752360. [[CrossRef](#)]
76. Ivarson, K.C. Microbiological formation of basic ferric sulfates. *Can. J. Soil Sci.* **1973**, *53*, 315–323. [[CrossRef](#)]
77. Tazaki, K.; Mori, T.; Nonaka, T. Microbial jarosite and gypsum from corrosion of Portland cement concrete. *Can. Miner.* **1992**, *30*, 431–444.
78. Farkas, I.M. Environmental Mineralogical and Geochemical Studies on the Bányabérc Waste Dump in the GyöngyöSOROSZI Mining Area, Hungary. Ph.D. Dissertation, Faculty of Science, Eötvös Loránd University, Budapest, Hungary, 2012.
79. Labrado, A.L.; Brunner, B.; Bernasconi, S.M.; Peckmann, J. Formation of Large Native Sulfur Deposits Does Not Require Molecular Oxygen. *Front. Microbiol.* **2019**, *10*, 24. [[CrossRef](#)]
80. Chaudhuri, S.K.; Lack, J.G.; Coates, J.D. Biogenic Magnetite Formation through Anaerobic Biooxidation of Fe(II). *Appl. Environ. Microbiol.* **2001**, *67*, 2844–2848. [[CrossRef](#)]
81. Piepenbrock, A.; Dippon, U.; Porsch, K.; Appel, E.; Kappler, A. Dependence of microbial magnetite formation on humic substance and ferrihydrite concentrations. *Geochim. Cosmochim. Acta* **2011**, *75*, 6844–6858. [[CrossRef](#)]
82. Polgári, M.; Hein, J.; Vigh, T.; Szabó-Drubina, M.; Fórizs, I.; Bíró, L.; Müller, A.; Tóth, A. Microbial processes and the origin of the Úrkút manganese deposit, Hungary. *Ore Geol. Rev.* **2012**, *47*, 87–109. [[CrossRef](#)]
83. Baele, J.M.; Bouvain, F.; De Jong, J.; Matielli, N.; Papier, S.; Préat, A. Iron microbial mats in Modern and Phanerozoic environments. In *Instruments, Methods, and Missions for Astrobiology XI*; International Society for Optics and Photonics: Washington, DC, USA, 2008; Volume 7097, p. 70970N12.
84. Konhauser, K.O. Diversity of bacterial iron mineralization. *Earth-Sci. Rev.* **1998**, *43*, 91–121. [[CrossRef](#)]
85. Schwertmann, U.; Cornell, R.M. *Iron Oxides in the Laboratory: Preparation and Characterization*; John Wiley & Sons: Hoboken, NJ, USA, 2007.
86. McGaw, I.J.; Curtis, D.L. A review of gastric processing in decapod crustaceans. *J. Comp. Physiol. B* **2012**, *183*, 443–465. [[CrossRef](#)] [[PubMed](#)]
87. Zbinden, M.; Gallet, A.; Szafranski, K.M.; Machon, J.; Ravoux, J.; Léger, N.; Duperron, S. Blow Your Nose, Shrimp! Unexpectedly dense bacterial communities occur on the antennae and antennules of hydrothermal vent shrimp. *Front. Mar. Sci.* **2018**, *5*, 357. [[CrossRef](#)]
88. Zbinden, M.; Cambon-Bonavita, M. *Rimicaris exoculata*: Biology and ecology of a shrimp from deep-sea hydrothermal vents associated with ectosymbiotic bacteria. *Mar. Ecol. Prog. Ser.* **2020**, *652*, 187–222. [[CrossRef](#)]
89. Guri, M.; Durand, L.; Cuffe-Gauchard, V.; Zbinden, M.; Crassous, P.; Shillito, B.; Cambon-Bonavita, M.-A. Acquisition of epibiotic bacteria along the life cycle of the hydrothermal shrimp *Rimicaris exoculata*. *ISME J.* **2012**, *6*, 597–609. [[CrossRef](#)]

- 
90. Apremont, V.; Cambon-Bonavita, M.-A.; Cueff-Gauchard, V.; François, D.; Pradillon, F.; Corbari, L.; Zbinden, M. Gill chamber and gut microbial communities of the hydrothermal shrimp *Rimicaris chacei* Williams and Rona 1986: A possible symbiosis. *PLoS ONE* **2018**, *13*, e0206084. [[CrossRef](#)]
  91. Vermeij, G.J. The Mesozoic marine revolution: Evidence from snails, predators and grazers. *Paleobiology* **1977**, *3*, 245–258. [[CrossRef](#)]

**Disclaimer/Publisher’s Note:** The statements, opinions and data contained in all publications are solely those of the individual author(s) and contributor(s) and not of MDPI and/or the editor(s). MDPI and/or the editor(s) disclaim responsibility for any injury to people or property resulting from any ideas, methods, instructions or products referred to in the content.